UVIT Observations of the Small Magellanic Cloud: Point-source Catalog

A. Devaraj[1,2] , P. Joseph[1,2] , C. S. Stalin[1] , S. N. Tandon[3] , and S. K. Ghosh[4]

[1] Indian Institute of Astrophysics, Bangalore, Karnataka, 560034, India; ashidevaraj@gmail.com
[2] Department of Physics and Electronics, CHRIST (Deemed to be University), Bangalore, Karnataka, 560029, India
[3] Inter-University Center for Astronomy and Astrophysics, Pune, Maharashtra, 411007, India
[4] Tata Institute of Fundamental Research, Mumbai, Maharashtra, 400005, India

Abstract

Three fields in the outskirts of the Small Magellanic Cloud were observed by the UltraViolet Imaging Telescope (UVIT) on board AstroSat, between 2017 December 31 and 2018 January 1. The observations were carried out on a total of seven filters, three in the far-ultraviolet (FUV; 1300–1800 Å) band and four in the near-ultraviolet (NUV; 2000–3000 Å) band. We carried out photometry of these observations that have a spatial resolution better than $1\rlap{.}{''}5$. We present here the first results of this work, which is a matched catalog of 11,241 sources detected in three FUV and four NUV wavelengths. We make the catalog available online, which would be of use to the astronomical community to address a wide variety of astrophysical problems. We provide an expression to estimate the total count rate in the full point-spread function of UVIT that also incorporates the effect of saturation.

Unified Astronomy Thesaurus concepts: Ultraviolet astronomy (1736); Ultraviolet telescopes (1743); Ultraviolet photometry (1740); Ultraviolet sources (1741)

Supporting material: machine-readable table

1. Introduction

Small Magellanic Cloud (SMC) is one of the closest ($D = 61.9 \pm 0.6$ kpc; Grijs & Bono 2015) star-forming galaxies to our galaxy (Hilditch et al. 2005). It has a low metallicity with $Z = 0.005$ (Dufour 1984) and low foreground extinction of $E(B-V) = 0.02$ mag (Hutchings 1982). The 2175 Å bump is absent in SMC which could be due to the dust in SMC being different from either the Milky Way or the Large Magellanic Cloud (LMC). Moreover, this has been attributed to the lack of carbonaceous dust (Weingartner & Draine 2001). SMC has been surveyed at various wave bands such as the near-infrared by the Two Micron All Sky Survey (2MASS; Cohen et al. 2003) in the mid and far-infrared by Spitzer (Gordon et al. 2011) and in the optical (Massey 2002). These observations indicate that SMC can be a unique laboratory to investigate stellar evolution and interstellar matter at low metallicity environments. SMC has also been targeted for observations in the X-ray band for studies on the X-ray binary population in low metallicity conditions (Lazzarini et al. 2019). In spite of the various multiwavelength observations available on SMC, the effect of its low metallicity appears most significant in the ultraviolet band (UV; Cornett et al. 1997). For example, as the spectral energy distribution of hot stars peaks at short wavelengths, far-ultraviolet (FUV) observations are important to determine the temperature of those hot stars compared to optical or infrared photometry. Though observations of SMC in the UV bands are highly important, a complete census of point sources (at a resolution similar to that available in the optical and near-infrared) is missing. SMC has been observed in the past by the Hubble Space Telescope (HST), the ultraviolet imaging telescope (UIT) flown on Space shuttle during Astro-1, Astro-2 missions (Cornett et al. 1994, 1997) and Swift/ UVOT (Hagen et al. 2017). The region of SMC to a large extent has been covered by the Galaxy Evolution Explorer (GALEX; Simons et al. 2014), though only in the near-ultraviolet (NUV) band (1771–2831 Å) with a spatial resolution of around $5''$. Though UIT observations are at a better spatial resolution ($3''$) than GALEX, such observations both in FUV and NUV are available only for limited regions of SMC. There is thus a need to improve the coverage and depth of the observations of SMC in both the FUV and NUV bands.

The UltraViolet Imaging Telescope (UVIT) on board India's multiwavelength astronomy satellite called AstroSat (Agrawal 2006) was launched on 2015 September 28. UVIT observes simultaneously in the FUV (1300–1800 Å) and NUV (2000–3000 Å) bands (Tandon et al. 2020) and provides better resolution images than GALEX and UIT. The main motivation of this work is to provide a point-source catalog for about 1/4 square degree of SMC field in multiple narrower filters in FUV and NUV at a resolution comparable to typical ground-based observations in the visible band. The observations and data reduction are described in Section 2, the generation of the point-source catalog is given in Section 3 followed by the summary in Section 4.

2. Observations and Reductions

The observations used in this work were taken by UVIT. UVIT consists of two 38 cm telescopes, one telescope for FUV and the second telescope for both NUV and VIS (3200–5500 Å) wavelengths. It has a circular field of view of $28'$ diameter and provides images with spatial resolution better than $1\rlap{.}{''}5$. It also has several filters in each of the channels (Tandon et al. 2020). The VIS channel is primarily used for tracking the aspect of the telescope during observation and applying offline corrections for spacecraft drift and other disturbances.

Three SMC fields were observed by UVIT between 2017 December 31 and 2018 January 1 (see Table 1 for details).

Figure 1. An RGB mosaic image of SMC-1, SMC-2, and SMC-3 fields. Here, red, green, and blue refer to the observations made in N263M, N245M, and F154W filters respectively.

Table 1
Log of Observations

| Field | Field Center | | Date | F154W | Exposure Time in Seconds for Different Filters | | | | | | |
	α_{2000}	δ_{2000}			F169M	F172M	N245M	N263M	N279N	N219M
SMC-1	01:09:46.0	−71:20:30.0	31-12-2017	1995	2825	4982	2010	2011	3017	2878
SMC-2	01:08:26.0	−71:20:30.0	01-01-2018	2004	2953	5019	2028	2067	2978	2996
SMC-3	01:09:46.0	−71:26:30.0	01-01-2018	1993	2432	4810	2009	2011	2854	2425

Table 2
Details of the Filters Used for the Observations

Filter	$\lambda_{mean}(\text{Å})$	$\Delta\lambda(\text{Å})$	Zero-point Magnitude
F154W	1541	380	17.771 ± 0.01
F169M	1608	290	17.410 ± 0.01
F172M	1717	125	16.274 ± 0.02
N245M	2447	280	18.452 ± 0.01
N263M	2632	275	18.146 ± 0.01
N279N	2792	90	16.416 ± 0.01
N219M	2196	270	16.654 ± 0.02

These exposures were used primarily to find flat-field variations across the 20′ field of view, for all the detector-filter combinations in NUV and FUV. The results of these are given in Tandon et al. (2020).

The first field (SMC-1) was selected far away from the central part of SMC so as to avoid the bright central regions of SMC and centered at $\alpha_{2000} = 01{:}09{:}46$ and $\delta_{2000} = -71{:}20{:}30.0$. The second (SMC-2) and third (SMC-3) fields were pointed to by applying a shift of ∼6′ in orthogonal

directions. A total of seven filters were used for the observations. Figure 1 shows the RGB image of the three fields. The details of the observations are given in Table 1. The effective wavelength and the bandwidth of the filters used in this work are given in Table 2. More details such as the effective areas of these filters can be found in Tandon et al. (2017, 2020).

The observed images of SMC were reduced using the UVIT L2 pipeline version 6.3 (Ghosh et al. 2021, 2022). This pipeline corrects the observations for geometric distortion, flat field as well as spacecraft drift. The spacecraft drift was obtained by tracking stars in the field of the VIS channel observations which was then applied to the data acquired in the FUV and NUV channels. The pipeline also performs astrometry of the final images using UV and optical catalogs. The final output of the L2 pipeline is a set of science-ready images that includes orbit-wise images as well as combined images, wherein the orbit-wise images (matched filter-wise) are stacked to get better S/N. The central 2′ × 2′ region of SMC-1 observed by UVIT and GALEX is shown in Figure 2 for comparison of resolution.
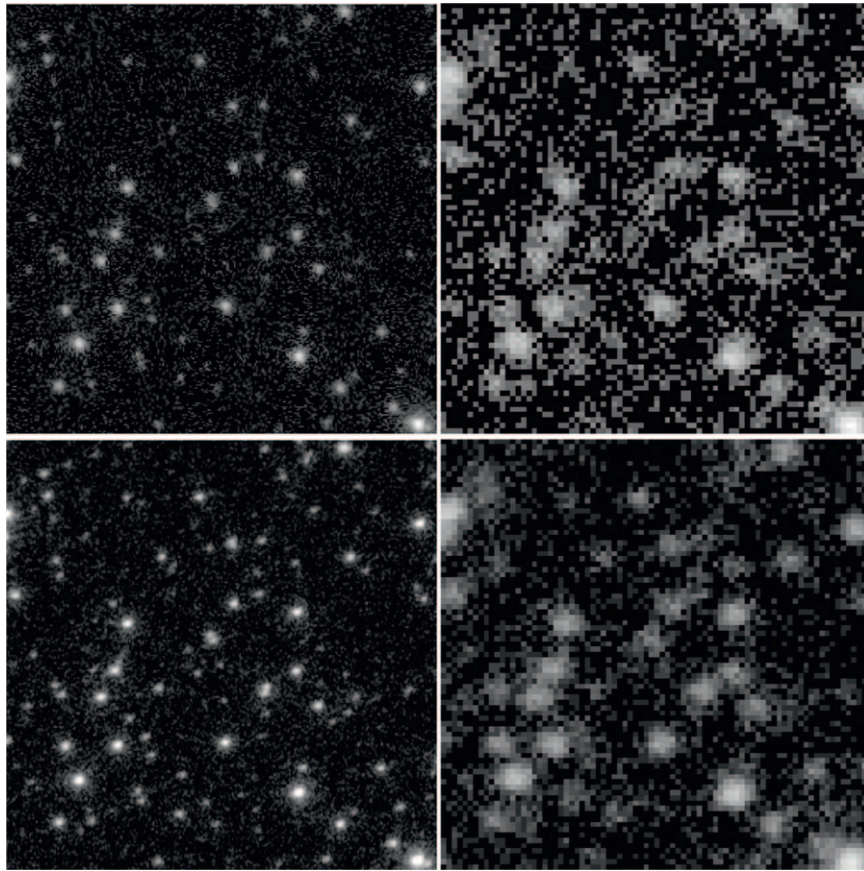
Figure 2. A $2' \times 2'$ region of SMC-1 centered at $\alpha = 01{:}09{:}46.0$, $\delta = -71{:}20{:}30.0$. The top left panel shows the UVIT FUV image in F154W filter, while the top right panel is the GALEX FUV image. The bottom panels show the image of the same region in UVIT NUV in the N245M filter (left panel) and in GALEX NUV (right panel).

From Figure 2, it is evident that the UVIT image has better resolution than GALEX thereby enabling the photometry of more point sources than that possible on the image from GALEX. The astrometry of the final combined images returned by the L2 pipeline is better than a few arcseconds, however, to improve the astrometry of UVIT images, we proceeded as follows. Using Aladdin,[5] we displayed the GALEX image of each of the SMC fields and overlaid the Gaia catalog. From this we visually identified 10 isolated stars in each of the SMC fields spread over the UVIT field of view. For those 10 stars (in each field) we found the (x,y) centroid positions in UVIT images and their corresponding (α,δ) from Gaia Data Release 2 (Gaia Collaboration et al. 2018). The selected stars have negligible proper motion (< 0.88 mas/yr). This information was used in the CCMAP routine in IRAF[6] to arrive at the transformation between (x,y) and (α,δ) that also includes rotation. This transformation was then applied to the UVIT images using CCSETWCS in IRAF, to arrive at the UVIT images with the new World Coordinate System (WCS). For doing this, the image taken in the FUV band F154W was considered as the reference and all the other images (both in FUV and NUV) were aligned to it. The WCS of all the images was further refined by an iterative process to minimize the angular separation between Gaia and UVIT coordinates. The distribution of the angular separation between the UVIT (α, δ) values and the matched sources with respect to the Gaia (α, δ)

values are given in the top panel of Figure 3. The cumulative distribution of the same is given in the middle panel of Figure 3. It shows that about 90% of the sources match within $0.''4$. We note that for a separation of about $0.''4$, which includes more than 90% of the sources, the probability of chance matching with a Gaia source is $\sim 1/250$. For the highest separation listed, the probability increases to $\sim 1/25$. The bottom panel of Figure 3 shows the variation in the angular separation between UVIT and Gaia sources as a function of distance from the center of SMC-1. The angular separation does not show any variation with respect to distance from the center. A similar trend is also seen in SMC-2 and SMC-3.

3. Photometric Analysis

The final combined and astrometric corrected images were analyzed to get counts per second (CPS) for individual sources and these were then converted to the AB magnitudes as per the calibration given in Tandon et al. (2020). There are two steps involved in making the best estimate of counts per second for individual sources. These steps are (i) an estimation based on a fit to a standard point-spread function (PSF) to a small central part of the sources covering a radius of 3 subpixels for NUV and 4 subpixels for FUV. This was done to minimize any overlap with the neighboring sources in this crowded field and (ii) the application of a correction factor to this counts per second, to get the actual total counts per second in the full PSF. However, there is a small complication in this step. In the photon counting process used for UVIT, if multiple photons

---

[5] https://aladin.u-strasbg.fr/AladinLite/
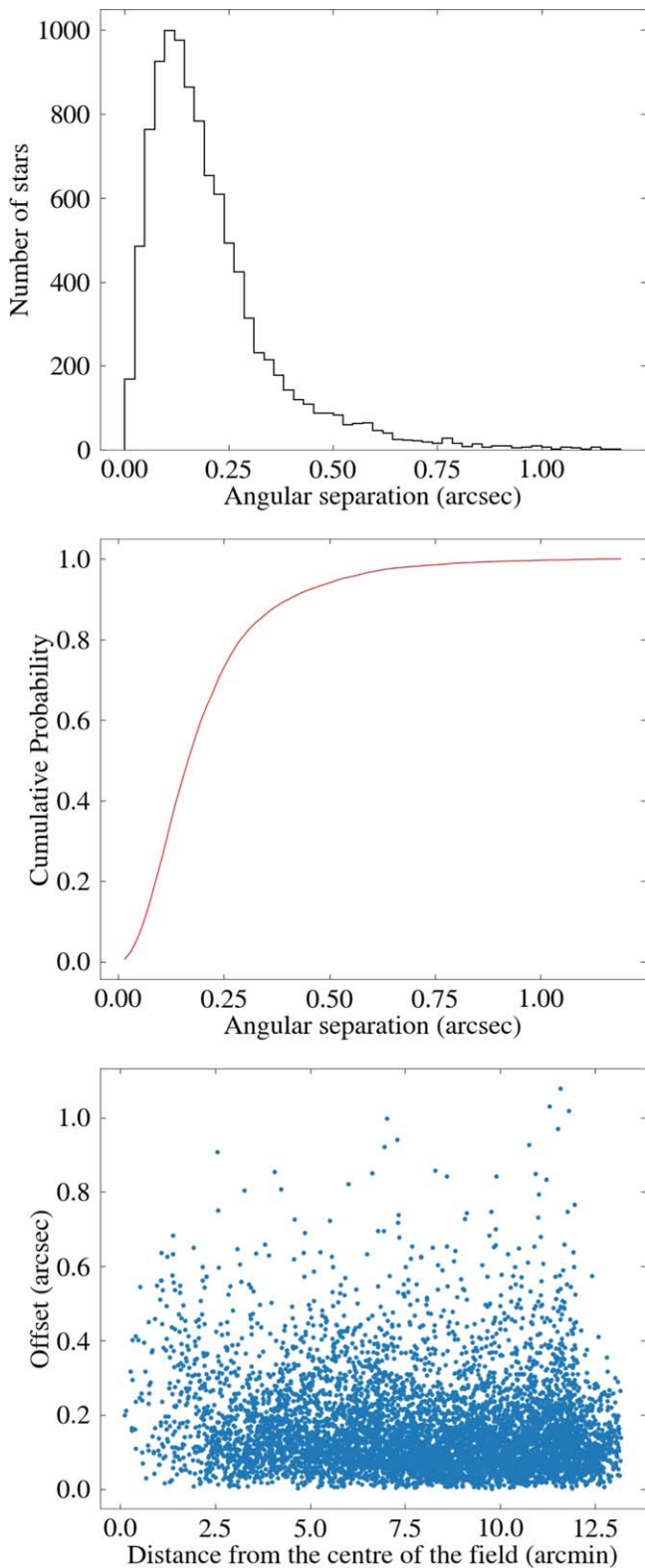[6] IRAF stands for Image Reduction and Analysis Facility.

Figure 3. The distribution of the angular separation between the sources in the UVIT SMC field crossmatched with the Gaia catalog is given in the top panel and the cumulative distribution function of the angular separation is shown in the middle panel. The offset in angular separation between UVIT and Gaia sources as a function of angular distance from the center of the SMC-1 field is shown in the bottom panel.

fall at the same location in any frame these are detected as a single photon. As the frame read rate is $\sim$29/s in full frame mode, the observed counts for a point source having 1 count

per second would suffer a saturation of $\sim$1.5%, and the saturation would increase with an increasing rate of counts. Thus, the correction factor for getting the actual total counts per second involves a correction for saturation too.

3.1. PSF Photometry

The procedure that was followed consisted of (i) finding point sources in the field, (ii) modeling the PSF and (iii) fitting the PSF model to each of the detected point sources to obtain the instrumental magnitude. This procedure was carried out using the DAOPHOT routines (Stetson 1987) implemented within IRAF. First, we detected all point sources using *daofind* in each of the images based on the threshold, $N \times \sigma_{\mathrm{back}}$. Here σ_{back} is the standard deviation of the local background in the field and N is the threshold. We set $N = 3$ for all the images. However, this resulted in many incorrect detections of faint sources. So we smoothed the images by convolving them with a Gaussian with a σ of 1.5 subpixels ($0.''62$), which led to improved source extraction. This improvement in detection after convolving with a Gaussian has also been noticed by Leahy et al. (2020) in their analysis of M31 images from UVIT. Once the sources were detected on the smoothed images through the *daofind* task in IRAF which uses the centroiding algorithm, photometry was performed on the original unsmoothed images using the positions of the point sources returned by *daofind* on the smoothed images. To model the PSF, among the detected point sources, we selected about 10 relatively isolated stars in each of the SMC fields. The PSF model generated using those 10 stars was fit to each of the point sources found by *daofind* to get the instrumental magnitudes and the associated errors in them. They were then converted to AB magnitudes using the zero-point magnitudes given in Tandon et al. (2020), and the errors in the AB magnitudes were obtained by error propagation (Bevington & Robinson 1992). Various functional forms were used to model the PSF in IRAF such as Gauss (elliptical Gaussian function), lorentz (elliptical Lorentzian function), moffat15 (elliptical Moffat function with a beta parameter of 1.5), and moffat25 (elliptical Moffat function with a beta parameter of 2.5); however, for generation of the final catalog we adopted the PSF modeled using the moffat25 function, since moffat25 gave minimum residuals while modeling the PSF compared to other functions.

3.2. Estimation of Total Count Rate in the Full PSF of UVIT

The counts obtained from the PSF fit to the point sources that needed to be corrected for the counts in the outer part of the PSF and for saturation. As correction for saturation is a bit involved, we first describe the correction for counts in the outer part of the PSF while assuming that there is no saturation. If there were isolated bright stars in the field, one could just find counts in a large aperture, e.g., in a radius of 30 subpixels which includes 97% of the total counts (see Tandon et al. 2020). However, in this crowded field suitably isolated stars are not available, and we took a two-step approach for this correction. First, we found a conversion factor for the ratio of PSF-fitted flux to the flux in a radius of 12 subpixels using a selection of bright stars, and second, we used the conversion factor given in Tandon et al. (2020) to convert the flux in a radius of 12 subpixels to the total flux in the full PSF (100 subpixels radius). The rationale for choosing the intermediate step of finding the relative flux in a radius of 12 subpixels is as
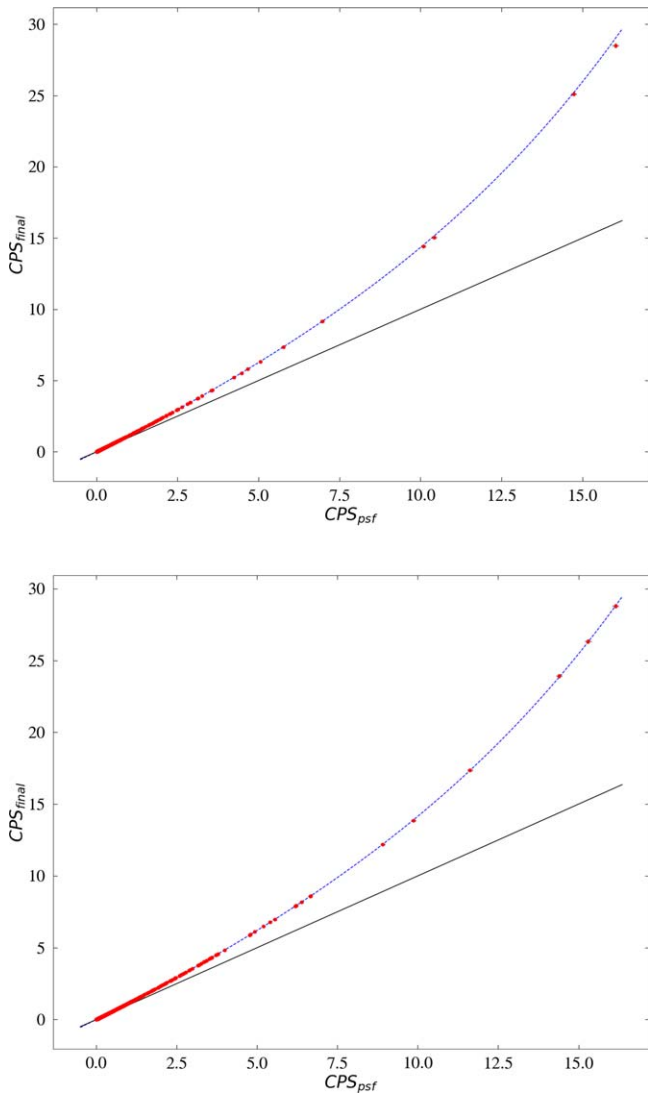
Figure 4. The correlation between the observed CPS from PSF fitting and the final corrected CPS for the FUV filter F154W (top panel) and the NUV filter N263M (bottom panel). The black solid line shows the $\mathrm{CPS_{psf}} = \mathrm{CPS_{final}}$ line, while the blue dashed line is the empirical model in Equation (2).

follows: the core of the PSF, to which the PSF fit is made, can change from image to image due to variations in errors in tracking the pointing and focus for individual filters, but the outer parts of the PSF are not affected by these small errors and thus the fractional energy contained within a radius of 12 subpixels is robust at ∼89% (see Tandon et al. 2020).

Before explaining the various factors involved in correcting for saturation, let us get a rough idea of its magnitude. A rough estimate of the saturation can be made by invoking Poisson statistics for the total counts per frame, which is equal to counts per second divided by 28.7 (the number of frames per second for the present observations). As the observed counts per frame are equal to "1− fraction of frames with no event/count," the saturation can be estimated from the following equation:

$$C = -\ln(1 - F) \qquad (1)$$

where C is the corrected total counts per frame and F is the fraction of frames with no event/count. However, the actual correction for saturation is less in the pedestal because the

Table 3
Coefficients in Equation (3)

Coefficient	FUV	NUV
a1	−0.003016	−0.002775
a2	0.024022	0.023266
a3	−0.000142	-9.669652×10^{-5}
a4	8.215584×10^{-5}	7.507352×10^{-5}

photons falling in the much less dense pedestal suffer very little saturation. To proceed further we followed the procedure described in Tandon et al. (2020). First, we assumed that all the saturation is limited within a radius of 12 subpixels and that there is no saturation in the outer parts of the PSF. Next, we assumed that the saturation factor is constant within the radius of 12 subpixels or the conversion factor from the PSF-fitted counts per second to the counts per second in the radius of 12 subpixels is unaffected by saturation. Given these two assumptions, for every value of PSF-fitted counts per second, the saturation-corrected total counts per second can be calculated from the equations for saturation and the detailed PSF given in Tandon et al. (2020). We found that the PSF-fitted counts per second and the total corrected counts per second are well fitted by the equation

$$\mathrm{CPS_{final}} = X \times \left(\frac{1}{\mathrm{CF}_{12}} + \mathrm{SAT}(X) \right). \qquad (2)$$

Here, $\mathrm{CPS_{final}}$ is the final corrected counts per second for the full PSF, $X = \mathrm{CPS_{PSF}} \times \mathrm{CF_{PSF12}}$, where $\mathrm{CPS_{PSF}}$ is the counts per second in the fitted PSF, $\mathrm{CF_{PSF12}}$ is the correction factor for correcting the PSF-fitted counts per second to counts per second in a radius of 12 subpixels. The first term on the right-hand side of Equation (2), gives the total counts per second without any correction for saturation, and the second term represents the correction for saturation. Values for the function SAT(X) are well fitted by the following polynomial of third order as given in Equation (3). The coefficients of this polynomial for NUV and FUV are given in Table 3 and the values for the conversion factor $\mathrm{CF_{PSF12}}$ for the various filters are given in Table 4. CF_{12} is the correction factor to covert the counts per second from 12 subpixels radius to counts per second in the full PSF (100 subpixels radius) is 0.893 for FUV and 0.886 for NUV (from Tandon et al. 2020).

$$\mathrm{SAT}(X) = a1 + a2 \times X + a3 \times X^2 + a4 \times X^3. \qquad (3)$$

Details of the procedure for the calculation of the function "SAT" are given in Appendix (also see Figure 4).

All the above discussion on saturation refers to the actual observed counts per second on the detector, while the counts per second in the images involve a correction for the flat field. Therefore, we first have to calculate the actual observed counts per second on the detector by applying the flat-field correction in reverse, calculate the total counts per second for this corrected rate and finally apply the flat-field correction to this corrected rate. The flat-field correction factor used for this is an average of its values over 21×21 subpixels (∼1″1 × 1″1) around the center of the source to account for drift during the pointing. Finally, we note that this correction for saturation is accurate to 5% for observed counts per second < 12 within a radius of 12 subpixels. We also note that we have neglected

Table 4
Aperture Correction and Flux Ratio in Different NUV and FUV Filters for Different PSF Fitting Models

Filter	No. of stars	Gauss		moffat25		moffat15		lorentz	
		AC	Ratio	AC	Ratio	AC	Ratio	AC	Ratio
F154W	81	-0.276 ± 0.004	1.290 ± 0.004	-0.299 ± 0.004	1.318 ± 0.005	-0.312 ± 0.004	1.333 ± 0.005	-0.335 ± 0.004	1.362 ± 0.004
F169M	109	-0.322 ± 0.003	1.346 ± 0.004	-0.335 ± 0.003	1.362 ± 0.004	-0.340 ± 0.003	1.369 ± 0.004	-0.349 ± 0.003	1.380 ± 0.004
F172M	72	-0.298 ± 0.004	1.317 ± 0.005	-0.311 ± 0.004	1.332 ± 0.005	-0.319 ± 0.004	1.342 ± 0.005	-0.336 ± 0.004	1.363 ± 0.005
N245M	114	-0.415 ± 0.004	1.467 ± 0.006	-0.417 ± 0.004	1.469 ± 0.006	-0.416 ± 0.004	1.468 ± 0.006	-0.429 ± 0.004	1.486 ± 0.006
N263M	110	-0.413 ± 0.005	1.465 ± 0.007	-0.416 ± 0.005	1.469 ± 0.007	-0.412 ± 0.005	1.463 ± 0.007	-0.434 ± 0.005	1.493 ± 0.007
N279N	49	-0.397 ± 0.007	1.442 ± 0.009	-0.405 ± 0.007	1.454 ± 0.009	-0.400 ± 0.007	1.447 ± 0.009	-0.432 ± 0.007	1.491 ± 0.009
N219M	75	-0.528 ± 0.007	1.629 ± 0.011	-0.531 ± 0.007	1.633 ± 0.011	-0.533 ± 0.007	1.636 ± 0.010	-0.544 ± 0.006	1.652 ± 0.010

Note. Flux ratio is the conversion factor (CF_{PSF12}) to convert the measured PSF Magnitudes to Magnitudes Obtained Over a Radius of 12 Subpixels.
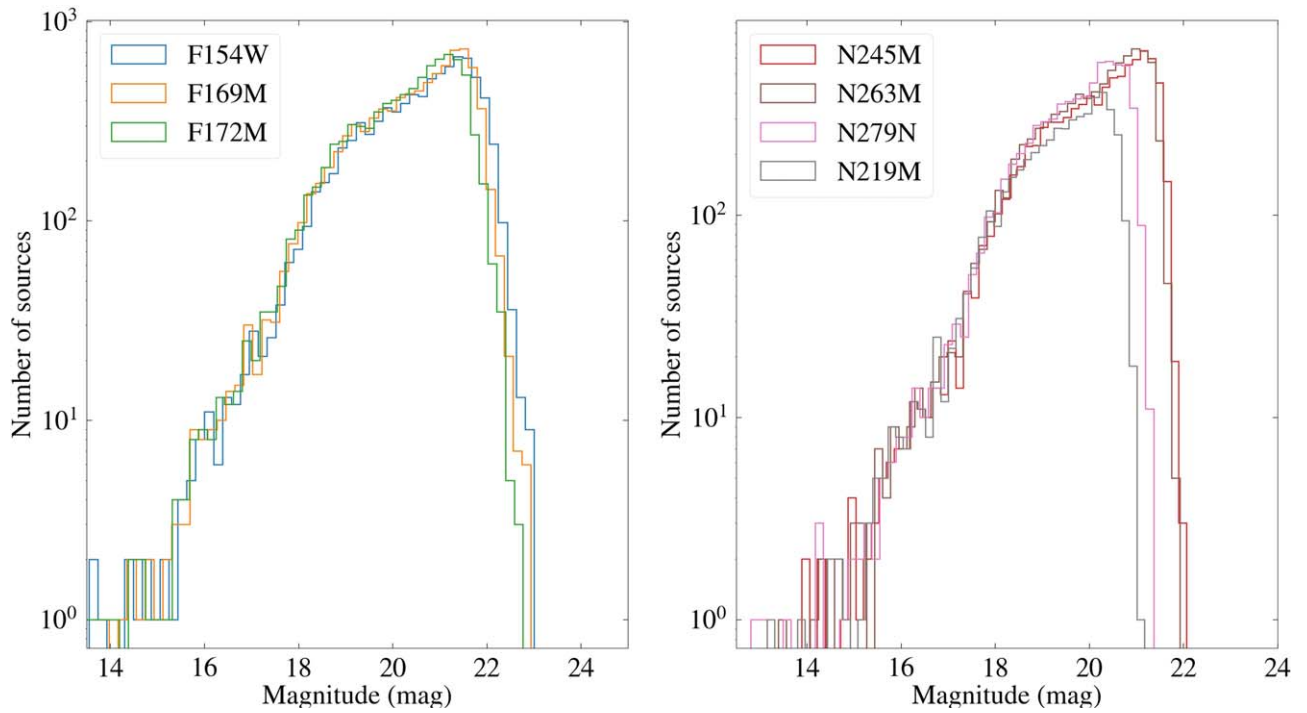
Figure 5. Distribution of AB magnitudes of the point sources in the SMC field for the three FUV (left panel) and four NUV (right panel) filters.

Table 5
Variation of Completeness of the Catalog with the Brightness of the Sources

Mag. Range	F154W	F169M	F172M	N245M	N263M	N279N	N219M
14–18	1.00	1.00	1.00	0.98	1.00	1.00	0.98
18–20	0.97	0.98	1.00	0.99	1.00	1.00	0.99
20–21	0.94	0.98	0.94	0.98	0.98	0.96	0.98
21–22	0.88	0.98	0.84	0.99	0.90	0.67	0.82
22–23	0.21	0.30	0.16	0.33	0.23	0.10	0.17
23–24	0.02	0.04	0.00	0.01	0.03	0.00	0.00

another saturation effect which is related to the saturation current in the MCP of the detector. This depends on the counts per second, and is estimated to be $< 5\%$ for 150 counts per second (see Tandon et al. 2020).

3.3. Completeness of the Catalog

We show in Figure 5 the magnitude distribution of the sources detected in the FUV and NUV filters. The peak of the magnitude distribution gives an approximate estimate of the completeness of the SMC observations. In the FUV band, for the filters F154W, F169M, and F172M we found the peak in the distribution of magnitudes at 21.30, 21.41, and 21.09 mag respectively. Similarly, for the NUV channel we found values of 21.08, 20.89, 20.34, and 20.21 mag respectively for the filters N245M, N263M, N279N, and N219M. The variation of error as a function of brightness for all the filters is shown in Figure 6. The errors show a sharp increasing trend after magnitudes that roughly correspond to the peak of the distribution in Figure 5.

We also assessed the completeness of our photometry as a function of brightness by introducing artificial stars. We added artificial stars numbering about 10% of the point sources

detected in each of the filters. The preselected positions and brightness were added randomly (using the addstar routine in IRAF) to each of the filters, so as not to alter the crowding characteristics. After the addition of the artificial stars, the photometry of the frames was carried out in the usual procedure (see Section 3.1). The ratio of the number of recovered stars to that inserted gives a measure of the completeness of our photometry. The variation of the completeness factor as a function of brightness for different filters is given in Table 5 and shown in Figure 7.

4. Summary

In this work, we have analyzed three pointings of SMC, observed by UVIT. From this analysis, we arrived at a catalog of 11,241 UV sources in the three fields of SMC, and provided their AB magnitudes in a total of seven filters, three in FUV and four in NUV. The sample catalog of 15 sources is given in Table 6. The full catalog is available in the electronic version of the article. This catalog will be of use to the astronomical community to address a large range of astronomical problems. We also carried out an evaluation of the relation between observed and saturation-corrected UVIT magnitudes. We found

Table 6
Sample from the Matched Catalog of Point Sources in SMC in Three FUV and Four NUV Filters

S. No.	α_{2000} (deg)	δ_{2000}(deg)	F154W		F169M		F172M		N245M		N263M		N279N		N219N	
			AB	Error	AB	Error	AB	Error	AB	Error	AB	Error	AB	Error	AB	Error
1	17.483551	−71.477719	19.274	0.049	19.206	0.047	19.194	0.059	19.127	0.033	19.034	0.036	18.999	0.065	18.992	0.059
2	17.501380	−71.474138	19.861	0.064	19.638	0.057	19.817	0.079	19.870	0.047	19.655	0.049	19.612	0.086	19.354	0.070
3	17.411340	−71.473069	21.085	0.112	21.079	0.111	20.556	0.111	20.625	0.066	20.402	0.068	20.453	0.127	20.244	0.106
4	17.516082	−71.469507	16.307	0.012	16.281	0.012	16.355	0.016	16.361	0.009	16.322	0.010	16.377	0.019	16.217	0.017
5	17.426452	−71.468917	20.073	0.070	20.053	0.069	19.800	0.078	19.392	0.037	19.257	0.040	19.223	0.072	19.383	0.071
6	17.546273	−71.468802	20.399	0.082	20.105	0.071	20.354	0.101	20.214	0.055	20.149	0.061	20.020	0.104	20.007	0.095
7	17.442353	−71.467313	20.776	0.097	20.816	0.098	20.722	0.119	20.704	0.068	20.415	0.069	20.343	0.121	20.348	0.111
8	17.218003	−71.463924	21.673	0.147	21.519	0.135	21.242	0.152	20.926	0.076	20.469	0.071	19.995	0.103	20.581	0.123
9	17.332593	−71.463868	19.558	0.055	19.511	0.054	19.564	0.070	19.589	0.041	19.494	0.045	19.235	0.072	19.401	0.072
10	17.548006	−71.462470	19.460	0.053	19.380	0.051	19.239	0.060	19.085	0.032	18.945	0.035	18.877	0.061	19.004	0.060
11	17.657541	−71.459780	21.125	0.114	21.621	0.142	21.294	0.155	21.068	0.081	20.820	0.083	20.774	0.147	20.699	0.130
12	17.542935	−71.458877	21.101	0.113	21.374	0.127	20.951	0.133	20.993	0.078	20.598	0.075	20.195	0.113	20.533	0.121
13	17.443856	−71.458562	21.740	0.151	21.481	0.133	21.444	0.166	21.265	0.088	21.284	0.103	20.749	0.145	20.726	0.132
14	17.666746	−71.456551	20.290	0.078	20.238	0.075	20.164	0.092	20.040	0.050	19.816	0.052	19.720	0.091	19.847	0.088
15	17.537647	−71.455490	20.427	0.083	20.316	0.078	20.184	0.093	20.267	0.056	19.953	0.056	19.913	0.099	20.157	0.102

Note. The table in full is available in the electronic version of the article.

(This table is available in its entirety in machine-readable form.)

(a) F154W

(b) F169M

(c) F172M
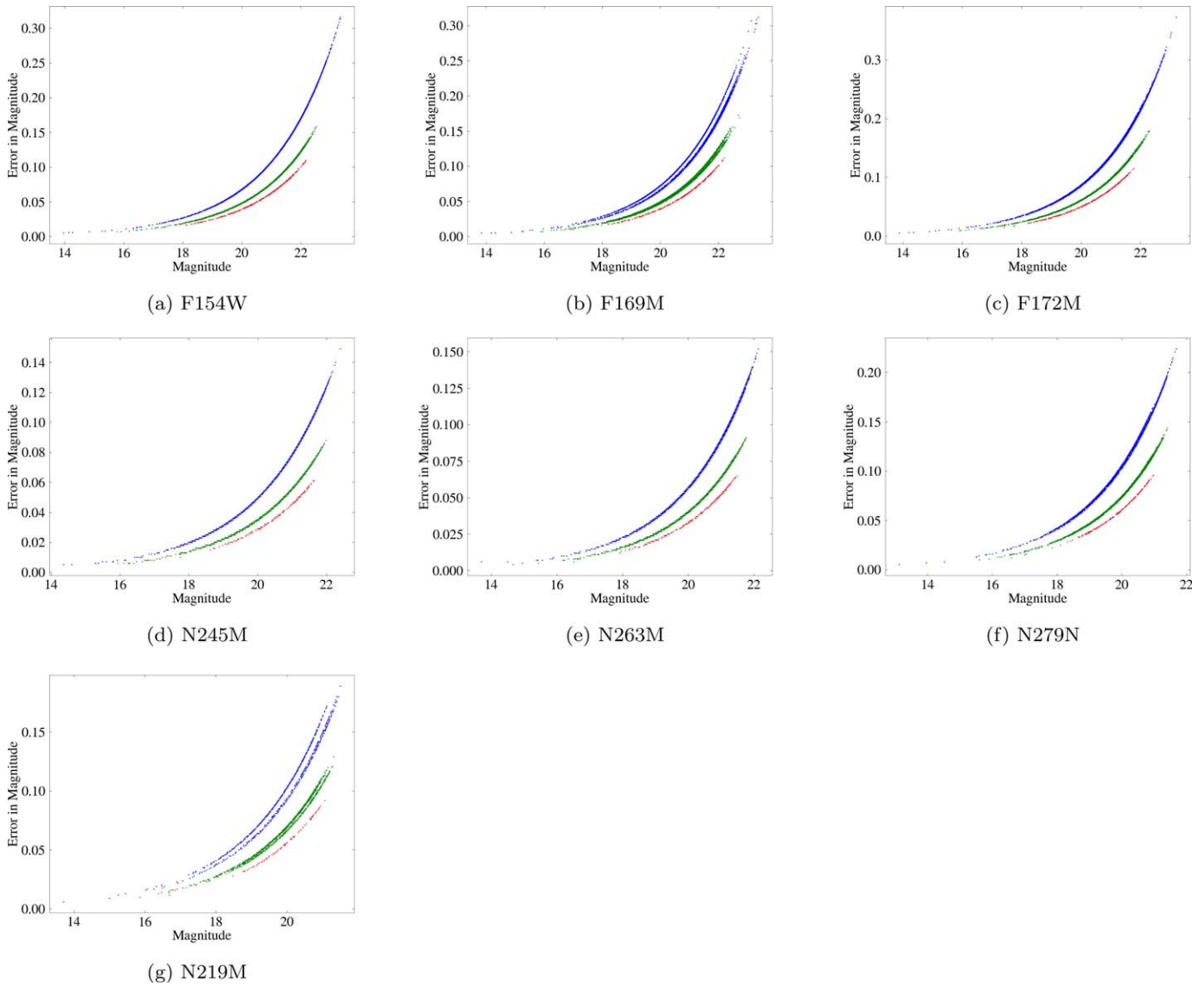
(d) N245M

(e) N263M

(f) N279N

(g) N219M

Figure 6. Error-magnitude plots for the detected sources in different filters. The three distinct bands in each filter correspond to sources common to all three pointings (red), common in two pointings (green), and present in each individual pointing (blue). The splitting seen in blue and green are due to the difference in exposure time between three different pointings (see Table 1).
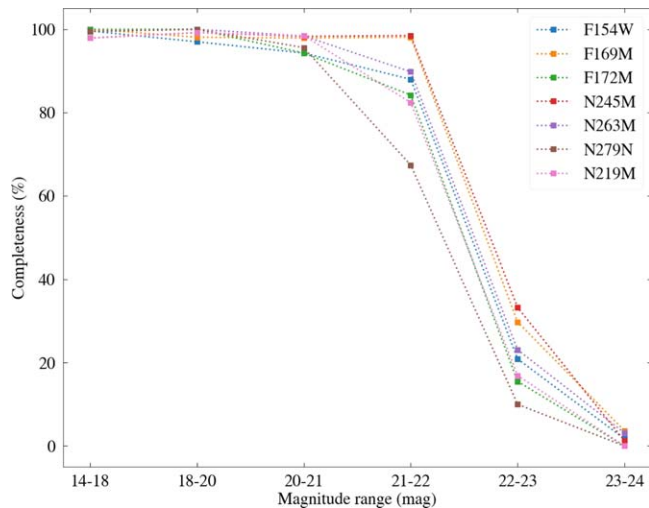

Figure 7. The completeness in percentage for different filters in the catalog.

that the observed UVIT magnitudes need to be corrected for the effects of saturation and PSF and provide empirical relations for the same.

Appendix
Saturation Correction

In the NUV and FUV channels of UVIT, the occurrence of multiple photon events within 3×3 pixels ($\sim 10'' \times 10''$) in a frame is detected as a single photon. Thus, for point sources with counts per frame >0.1, a significant number of photons are not recorded. This effect of saturation needs to be taken into account while estimating the brightness of point sources from the measured count rates. Another possible source of saturation is the reduced multiplication of the photoelectrons in the MCPs, reducing the final signal and hence reducing the probability of detection, when the local photon rate is high. However, this effect is estimated to be $<5\%$ for rates of 150 detected photons per second for a point source and has been ignored (Tandon et al. 2017). To correct for the effects of saturation, we adopted the empirical method outlined in Tandon et al. (2017). Essential steps in this method are: (i) assuming Poisson statistics for the occurrence of multiple photons in a frame for 97% of the counts per frame in the full PSF (CPF5), an ideal correction (ICORR) was calculated (97% is arbitrarily chosen to discard counts in the outermost part of the PSF), (ii) a relation (given in Equation (A1)) was derived relating the ideal correction to the actual correction found from detailed analysis of the frames, and (iii) the actual correction was used to find the corrected counts per frame and hence the corrected counts per second as given in Equation (A2).

$$RCORR = ICORR(0.89 - 0.30 \times ICORR^2) \qquad (A1)$$

$$CPS = (CPF5/0.97 + RCORR) \times 28.7. \qquad (A2)$$

Where 28.7 is the number of frames per second for the present observations. As we used the observed counts in a radius of 12 subpixels, the above process needs to be translated to obtain the corrected total counts per second from those observed in a radius of 12 subpixels. To do this, for various values of the corrected counts per second within the full PSF (CPS), the expected counts per second within a radius of 12 subpixels (CO12) were calculated as per the prescription in Equations (A1), (A2) and (A3). We also assumed that all the saturation is limited to a radius of 12 subpixels. The values of CPS were fitted to a third-order polynomial in CO12. This process is illustrated in the following equations:

$$CO12 = CPS \times CF_{12} - RCORR \times 28.7. \qquad (A3)$$

Here, CF_{12} is the correction factor to convert the counts per second in the full PSF (100 subpixels radius) to those in a radius of 12 subpixels in the absence of saturation, which is 0.893 for NUV and 0.886 for FUV (see Table 11 of Tandon et al. 2020).

We define a saturation correction factor SAT as per Equation (A4) and calculated SAT and CO12 for various values of CPS in the range 0.6–17. Next, a polynomial fit was made relating SAT to CO12 as

$$CPS = CO12 \times \left(\frac{1}{CF_{12}} + SAT \right) \qquad (A4)$$

$$\begin{aligned} SAT(CO12) = a1 + a2 \times CO12 + a3 \\ \times CO12^2 + a4 \times CO12^3 \end{aligned} \qquad (A5)$$

The coefficients of Equation (A5) are given in Table 3.

ORCID iDs

A. Devaraj ⓘ https://orcid.org/0000-0001-5933-058X
P. Joseph ⓘ https://orcid.org/0000-0003-1409-1903
C. S. Stalin ⓘ https://orcid.org/0000-0002-4998-1861
S. N. Tandon ⓘ https://orcid.org/0000-0001-6350-7421
S. K. Ghosh ⓘ https://orcid.org/0000-0003-0329-2160

References

Agrawal, P. C. 2006, AdSpR, 38, 2989
Astropy Collaboration, Robitaille, T. P., Tollerud, E. J., et al. 2013, A&A, 558, A33
Bevington, P. R., & Robinson, D. K. 1992, Data reduction and error analysis for the physical sciences (New York: McGraw-Hill)
Cohen, M., Wheaton, W., & Megeath, S. T. 2003, AJ, 126, 1090
Cornett, R. H., Greason, M. R., Hill, J. K., Parker, J. W., & Waller, W. H. 1997, AJ, 113, 1011
Cornett, R. H., Hill, J. K., Bohlin, R. C., et al. 1994, ApJL, 430, L117
Dufour, R. J. 1984, in IAU Symp. 108, Structure and Evolution of the Magellanic Clouds, ed. S. van den Bergh & K. S. D. de Boer (Cambridge: Cambridge Univ. Press), 353
Gaia Collaboration, Mignard, F., Klioner, S. A., et al. 2018, A&A, 616, A14
Ghosh, S. K., Tandon, S. N., Joseph, P., et al. 2021, JApA, 42, 29
Ghosh, S. K., Tandon, S. N., Singh, S. K., et al. 2022, JApA, 43, 77
Gordon, K. D., Meixner, M., Meade, M. R., et al. 2011, AJ, 142, 102
Grijs, R. d., & Bono, G. 2015, AJ, 149, 179
Hagen, L. M. Z., Siegel, M. H., Hoversten, E. A., et al. 2017, MNRAS, 466, 4540
Harris, C. R., Millman, K. J., van der Walt, S. J., et al. 2020, Natur, 585, 357
Hilditch, R. W., Howarth, I. D., & Harries, T. J. 2005, MNRAS, 357, 304
Hunter, J. D. 2007, CSE, 9, 90
Hutchings, J. B. 1982, ApJ, 255, 70
Lazzarini, M., Williams, B. F., Hornschemeier, A. E., et al. 2019, ApJ, 884, 2
Leahy, D. A., Postma, J., Chen, Y., & Buick, M. 2020, ApJS, 247, 47
Massey, P. 2002, ApJS, 141, 81
McKinney, W., et al. 2010, in Proc. the 9th Python in Science Conf. 445, ed. S. van der Walt & J. Millman, 5156
Simons, R., Thilker, D., Bianchi, L., & Wyder, T. 2014, AdSpR, 53, 939
Stetson, P. B. 1987, PASP, 99, 191
Tandon, S. N., Postma, J., Joseph, P., et al. 2020, AJ, 159, 158
Tandon, S. N., Subramaniam, A., Girish, V., et al. 2017, AJ, 154, 128
Tody, D. 1986, Proc. SPIE, 627, 733
Virtanen, P., Gommers, R., Oliphant, T. E., et al. 2020, NatMe, 17, 261
Weingartner, J. C., & Draine, B. T. 2001, ApJ, 548, 296